DE GRUYTER

Open Physics 2025; 23: 20250186

Research Article

Sivasankaran Sivanandam* and Turki J. Alqurashi

Activation energy and cross-diffusion effects on 3D rotating nanofluid flow in a Darcy–Forchheimer porous medium with radiation and convective heating

https://doi.org/10.1515/phys-2025-0186
received February 21, 2025; accepted June 17, 2025

Abstract: The goal of the current study is to discover the impact of cross diffusion effects, activation energy, thermal radiation, and convective heating on three-dimensional doubly diffusive convective nanoliquid flow over a rotating surface in a Darcy–Forchheimer porous domain with heat generation. The governing model (partial differential equations) are solved numerically after being converted by similarity transformation into a nonlinear ordinary differential system. The numerical solutions are obtained for various combinations of effects involved in the physical model. The skin friction and mass and heat transferral rates are also computed. The activation energy is more pronounced on solutal transport than that of on thermal transport. The heat transfer is suppressed by strengthening the values of the inertia parameter and the rotational parameter.

Keywords: activation energy, Soret/Dufour effect, radiation, rotating flow, Darcy–Forchheimer porous medium, convective heating

Nomenclature

a	constant
$\mathrm{Bi_c}$	solute Biot number
$\mathrm{Bi_T}$	thermal Biot number
C	solute concentration
Cf	skin friction
C_b	drag co-efficient
c_p	specific heat at constant temperature
c_s	concentration susceptibility
Df	Dufour parameter
D_m	solute diffusivity
D_T	thermophoretic diffusion coefficient
E	activation energy parameter
E_a	activation energy
f, g	non-dimensional velocities
F	inertia co-efficient
Fr	Forchheimer number
Hg	heat generation parameter
h_T	heat transfer coefficient
K_p	porous medium permeability
K_r	chemical reaction rate constant
k_T	thermal diffusion ratio
$k^{\#}$	mean absorption coefficient
n	fitted rate constant
Nb	Brownian motion parameter
Nt	thermophoresis parameter
Nu	Nusselt number
Pr	Prandtl number
q_r	heat flux due to thermal radiation
Q	heat generation
Re_x	Reynolds number
Rd	radiation parameter
Sc	Schmidt number
Sh	Sherwood number
Sr	Soret parameter
T	temperature
T_m	mean fluid temperature
u, v, w	velocities in x, y, z directions
x, y, z	Cartesian coordinates

Greek Letters

α_m	thermal diffusivity
β	rotational parameter

*** Corresponding author: Sivasankaran Sivanandam,** Mathematical Modelling and Applied Computation Research Group, Department of Mathematics, King Abdulaziz University, Jeddah, 21589, Saudi Arabia; Department of Mathematics, Saveetha School of Engineering, SIMATS, Chennai, 602105, Tamil Nadu, India, e-mail: sd.siva@yahoo.com

Turki J. Alqurashi: Department of Mathematics, Taif University, Taif, Saudi Arabia

δ	temperature difference parameter
ϕ	dimensionless solute concentration
η	similarity variable
λ	permeability parameter
ν	kinematic viscosity
θ	dimensionless temperature
ρ	density
σ^*	Stefan-Boltzmann constant
Ω	angular velocity

Subscripts

f	fluid
p	particle
w	conditions at surface
∞	conditions at free stream

1 Introduction

Heat energy transfer is crucial to many aspects of our daily life, from small-scale to large-scale applications. Through friction, chemical reactions (CRs), or electric losses, heat energy has been produced. Either all the heat must be removed (cooling) or it must be needed in specific areas as efficiently as feasible [1,2]. Thus, thermal management plays a vital role in an extensive range of technical applications, including bearing cooling in wind power plants, cooling electronics, and transportation (brake and radiator cooling) [3,4]. For optimal heat transfer, the medium needs to be highly conducive to efficient transmission. Because traditional media with low heat conductivity, such as water, synthetic oil, molten salt, and ethylene glycol, were developed, scientists created fluid–solid mixtures known as nanofluids [5–7]. In other words, liquids are blended with nanoscale (metallic, non-metallic, and polymeric) particles to improve their thermal characteristics and facilitate heat transfer [8–10]. Mandal and Pal [11] investigated the mixed convection flow of a hybrid nanofluid over an exponentially shrinking Riga surface. Their research focused on analyzing entropy generation and examining the stability of the flow.

The impact of CR and activation energy (AE) on the Casson nanoliquid stream flowing past a stretched surface with non-linear radiation was investigated by Gireesha *et al.* [12]. They investigated the effects of heat sources that are thermally dependent and exponentially space-dependent. Using the method of homotopy analysis, Vinodh *et al.* [13] identified magneto-hydrodynanic (MHD) Casson hybrid nanoliquid current over a moving needle under the impact of Dufour/Soret effects and thermal radiation. When the Casson parameter is raised by 20%, skin friction rises by up to 45%. In the occurrence of AE and CR, Acharya and Das [14] observed the incompressible MHD rotating hybrid-nanofluid (kerosene oil–Al_2O_3–Cu) flow over a stretchable sheet. They concluded that whereas temperature rises as radiation parameter values rise, the opposite phenomenon is seen for concentration when CR values rise. A radially stretched plate created a time-dependent, axisymmetric, chemically reactive Williamson nanofluid flow in the porous medium with Joule heating, AE, and viscous dissipation, according to Saini *et al.* [15]. The temperature is thought to rise with increasing Brownian motion and temperature ratio parameters, and to decrease with increasing velocity slip. The magneto-convection of a hybrid (methanol, CuO, and MgO) nanofluid flow was examined by Vijay and Sharma [16] using a spinning disk that was decelerating and included Ohmic heating, Soret, and Dufour consequences. Here, we take into consideration the temperature-dependent viscosity of hybrid nanoliquid. The influence of CR and Joule heating on a hybrid nanoliquid across a stretchy sheet with entropy generation is investigated by Joyce *et al.* [17]. They discovered that raising the slip parameter causes a hybrid nanofluid's flow rate to drop. Using the differential transform method, Chandrapushpam *et al.* [18] investigated double diffusive MHD squeezed nanoliquid flow in Darcy porous media in the occurrence of CR. They detected that the squeeze number supports mass transfer rate, and it reduces the skin friction when increasing the Biot number.

It is essential to comprehend AE, as it is a prerequisite for nearly all chemical processes. AE aids in our understanding of the energy required for a CR, which governs both the environment and our behaviour [19]. The AE with CR exists in mass and heat transport and has applications in emulsions of multiple suspensions, chemical technology, geothermal reservoirs, food and material processing, *etc.* [20,21]. The free convective boundary layer stream in porous media with simultaneous mass and heat transfer was studied by Bestman [22] with an AE and a CR. Huang [23] used the Keller box method to quantitatively assess the impact of Arrhenius AE on free convection around a permeable horizontal cylinder maintained at a constant wall concentration and temperature. The effects of the magnetic field, CR, and AE on nanofluid flow over a flexible disc were investigated by Kotresh *et al.* [24]. It is shown that higher solid volume fraction values improve the drag coefficient and reduce the heat transfer rate. Yesodha *et al.* [25] investigated the effects of AE and Dufour/Soret effects on the properties of mass and heat transfer of a chemically reacting viscous fluid in a rotating frame. They discovered that the Dufour and Soret parameters both result in a drop-in concentration. The mixed MHD convective non-Newtonian nanoliquid flow with AE and thermal radiation was studied by Younus and Lakshmi [26]. They discovered that local mass transfer decreases with increasing AE and increases with rising CR rate.

The Dufour effect describes how variations in solute concentration affect energy fluxes. The Soret effect refers to the solute fluxes that are impacted by temperature gradients [27]. The heat and solute transfer are accelerated by the emergence of cross diffusion (Dufour and Soret) effects [28–30]. The influence of Dufour and Soret effects on MHD convection stagnation-point stream of chemically reacting fluids with radiation and slip condition was inspected numerically by Niranjan *et al.* [31]. The problem of unsteady MHD convection of an electrically conducting liquid across an (inclined) plate immersed in a porous material in the existence of the Soret effect, a CR, a Hall current, and an aligned magnetic field was solved exactly analytically by Raghunath and Mohanaramana [32]. The Dufour and Soret effects on magneto-convection nanoliquid stream with slip and thermal radiation effects over a cylinder were studied by Jagan and Sivasankaran [33]. It is concluded that while local heat transmission decreases with increasing Dufour number, local mass transfer increases. Geetha *et al.* [34] evaluated the effects of Dufour and Soret on an MHD bioconvection stream in a channel with a CR. They discovered that increasing thermal radiation induces a progressive rise in heat transport.

In many technical applications, including power plants, re-entry vehicles, high-speed aircraft, and operations involving high temperatures, the impact of thermal radiation on convective flow is significant [35,36] (See, Sharma *et al.* [35,36], Yasmin *et al.* [37]). Numerous studies have extensively utilised of the radiative heat fluxes approximated by the Rosseland approximation. The nanoliquid flow *via* a vertical Riga plate in the occurrence of suction, slip, thermal radiation, and CR was described by Rawat *et al.* [38]. It was discovered that as thermal radiation improves, temperature and velocity also rise. The Casson fluid's entropy generation over an exponential stretchy surface with thermal radiation, heterogeneous-homogeneous reaction, and slip effects was evaluated by Das *et al.* [39]. They concluded that a rise in Brinkman number reduces the overall development of entropy. Sivasankaran *et al.* [40] explored the impact of thermal radiation on the buoyant convection of Casson fluid in a closed domain with various thermal sources. The effects of (linear and nonlinear) radiation on Maxwell fluid flow over a stretchy sheet with convective heating, AE, and viscous dissipation were investigated by Gangadhar *et al.* [41]. They concluded that as the Biot number rises, the thermal boundary layer improves. Mandal and Pal [42] investigated how thermal radiation influences the convective flow of a nanofluid when a uniform external magnetic field and slip condition are applied. The effects of radiation and CRs with continuous heat and mass flux of convective flow over a vertically placed plate in a porous medium were analytically explored by Choudhury and Sharma [43]. It is known that temperature and velocity decrease as radiation parameter increases. Additionally, it is discovered that when the radiation parameter values increase, the plate's internal friction decreases. Gangadhar *et al.* [44] conducted a numerical study on the influence of a magnetic field and thermal radiation on the flow of a second-grade nanofluid over a Riga plate with convective boundary heating. Their results showed that the temperature distribution increases with higher values of the radiation parameter and Biot number.

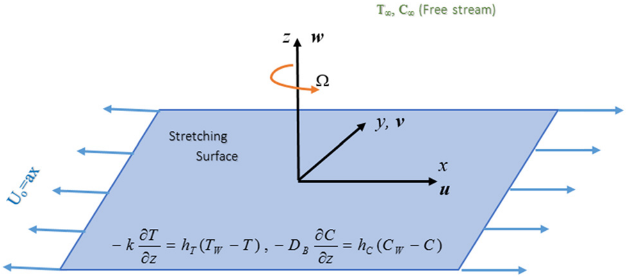

Figure 1: Physical model.

We can infer from the literature that no research has been conducted to examine how AE, radiation, Dufour, and Soret effects influence convective mass and heat transport. Therefore, these effects are investigated numerically in the current work on three-dimensional doubly diffusive rotating nanoliquid flow in Darcy–Forchheimer porous media in the presence of AE, radiation, Dufour, and Soret effects in a rotating surface.

2 Mathematical formulation

We consider a three-dimensional laminar, steady, incompressible flow over a rotating frame inserted into a porous medium as shown in Figure 1. The frame is rotating at an

Table 1: Comparison of skin friction values with Rd = Hg = Sr = Df = 0, Fr = 1, and β = 0.5

λ	$-f''(0)$		
	Present	**Rashid *et al.* [45]**	**Difference (%)**
0.1	1.4177152097	1.41806	0.0243
0.5	1.5302936158	1.53031	0.0011
1.0	1.6715382777	1.67153	0.0005

angular velocity “Ω.” The heat and solute transfer is included in the flow to examine the factors. The internal heat generation, thermo-diffusion (Soret effect), and diffusion-thermo (Dufour effect) effects (that is, the cross diffusion consequence) are included here. The thermal radiation is taken into account based on Rosseland approximation and the medium is optically thick. An AE-driven CR is taking place. The non-Darcy–Forchheimer porous model is taken and it supports the nonlinear flow behaviour with high velocities. The isotropic porous matrix is thermally equilibrium with local liquid. The surface of the plane $z = 0$ is stretched at a stretching rate $a(>0)$. The velocity components u, v, and w are located along the x, y, and z axes, respectively. Convective heating and salting are applied on the stretchy surface. The following assumptions are taken into the study.

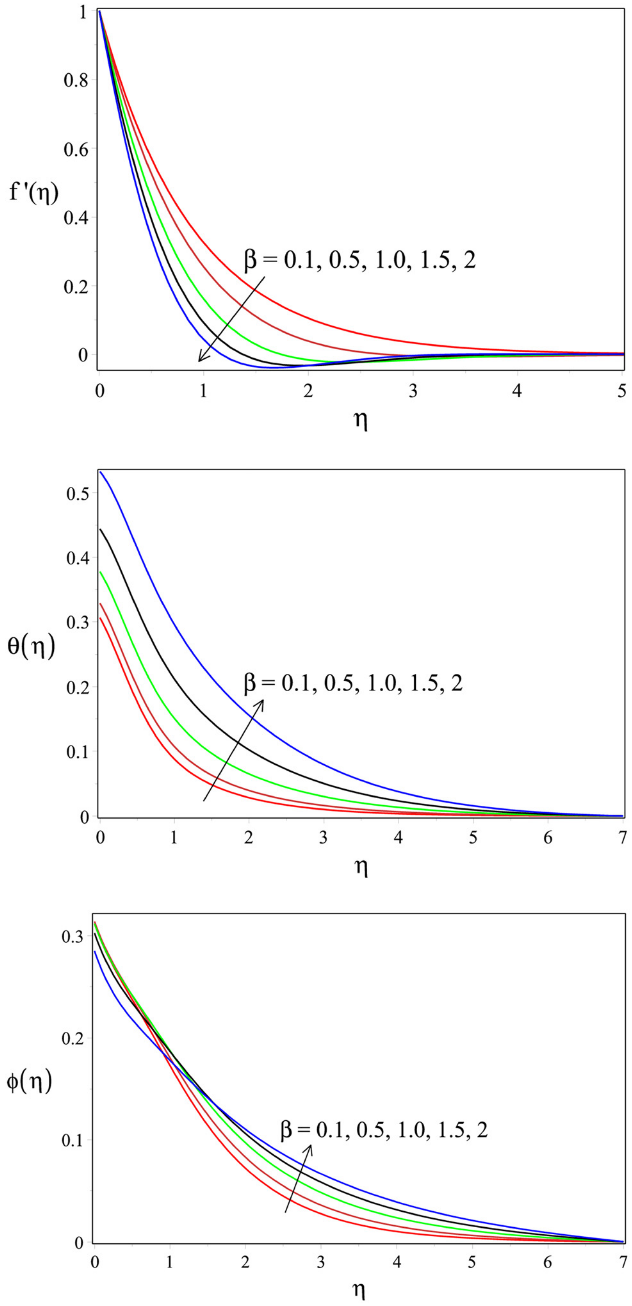

Figure 2: Velocity, temperature and concentration profiles for different values of β with Pr = 6.7, Sc = 1, λ = 0.2, E = 0.5, n = 0.5, Fr = 0.1, σ = 0.5, $\mathrm{Bi_T}$ = 0.3, $\mathrm{Bi_C}$ = 0.3, Hg = 0.1, δ = 0.5, Nb = 0.3, Nt = 0.1, Sr = 0.2, Df = 0.2 and Rd = 0.5.

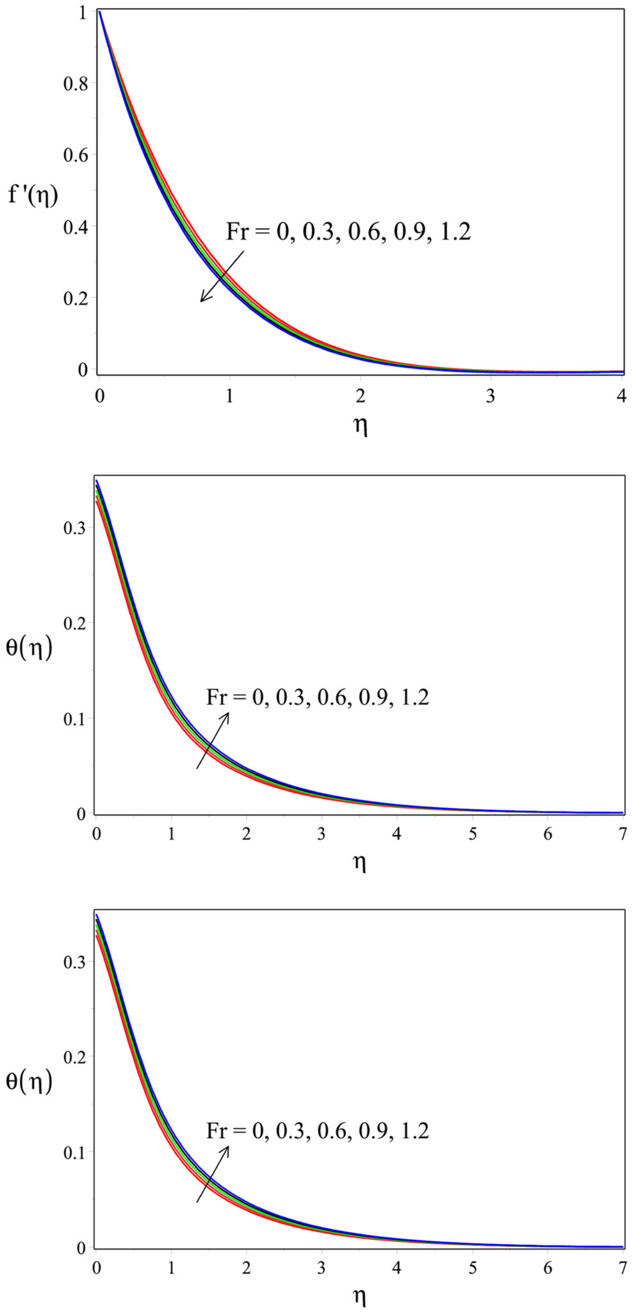

Figure 3: Velocity, temperature and concentration profiles for different values of Fr with Pr = 6.7, Sc = 1, λ = 0.2, E = 0.5, n = 0.5, β = 0.5, σ =0.5, $\mathrm{Bi_T}$ = 0.3, $\mathrm{Bi_C}$ = 0.3, Hg = 0.1, δ = 0.5, Nb = 0.3, Nt = 0.1, Sr = 0.2, Df = 0.2 and Rd = 0.5.

- The flow is incompressible, steady, and laminar.
- The surface is stretched with uniform velocity U_0.
- The porous medium is isotropic and thermally equilibrium with local fluid.
- The medium is optically thick and thermal radiation is considered.
- The AE-driven CR is taking place.

The governing models are [45]:

$$\frac{\partial u}{\partial x} + \frac{\partial v}{\partial y} + \frac{\partial w}{\partial z} = 0, \tag{1}$$

$$u\frac{\partial u}{\partial x} + v\frac{\partial u}{\partial y} + w\frac{\partial u}{\partial z} - 2\Omega v = \upsilon\frac{\partial^2 u}{\partial z^2} - \frac{\upsilon}{K_p}u - Fu^2, \tag{2}$$

$$u\frac{\partial v}{\partial x} + v\frac{\partial v}{\partial y} + w\frac{\partial v}{\partial z} + 2\Omega v = \upsilon\frac{\partial^2 v}{\partial z^2} - \frac{\upsilon}{K_p}v - Fv^2, \tag{3}$$

$$\begin{aligned} &u\frac{\partial T}{\partial x} + v\frac{\partial T}{\partial y} + w\frac{\partial T}{\partial z} \\ &= \alpha_m\frac{\partial^2 T}{\partial z^2} + \frac{(\rho c)_p}{(\rho c)_f}\left[D_m\left(\frac{\partial T}{\partial z}\frac{\partial C}{\partial z}\right) + \frac{D_T}{T_\infty}\left(\frac{\partial T}{\partial z}\right)^2\right] \\ &+ \frac{D_m k_T}{c_s c_p}\frac{\partial^2 C}{\partial z^2} - \frac{1}{(\rho c_p)_f}\frac{\partial q_r}{\partial y} + \frac{Q}{(\rho c_p)_f}(T - T_\infty), \end{aligned} \tag{4}$$

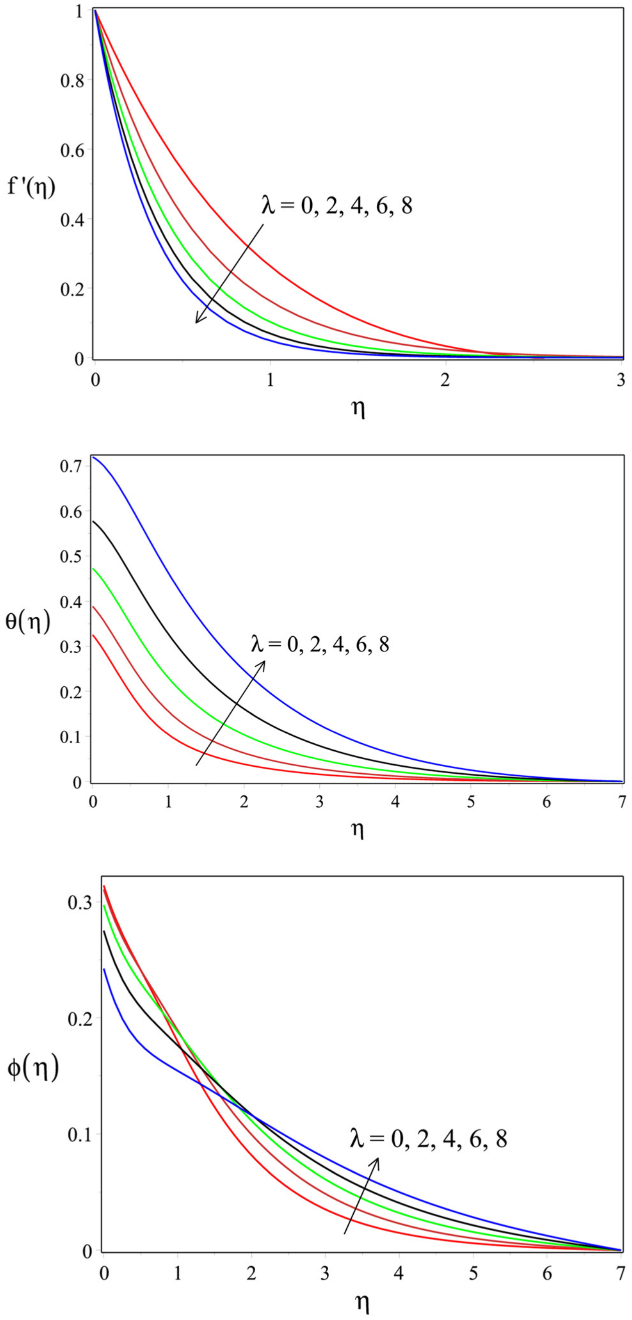

Figure 4: Velocity, temperature and concentration profiles for different values of λ with Pr = 6.7, Sc = 1, Fr = 0.2, E = 0.5, n = 0.5, β = 0.5, σ = 0.5, Bi_T = 0.3, Bi_C = 0.3, Hg = 0.1, δ = 0.5, Nb = 0.3, Nt = 0.1, Sr = 0.2, Df = 0.2 and Rd = 0.5.

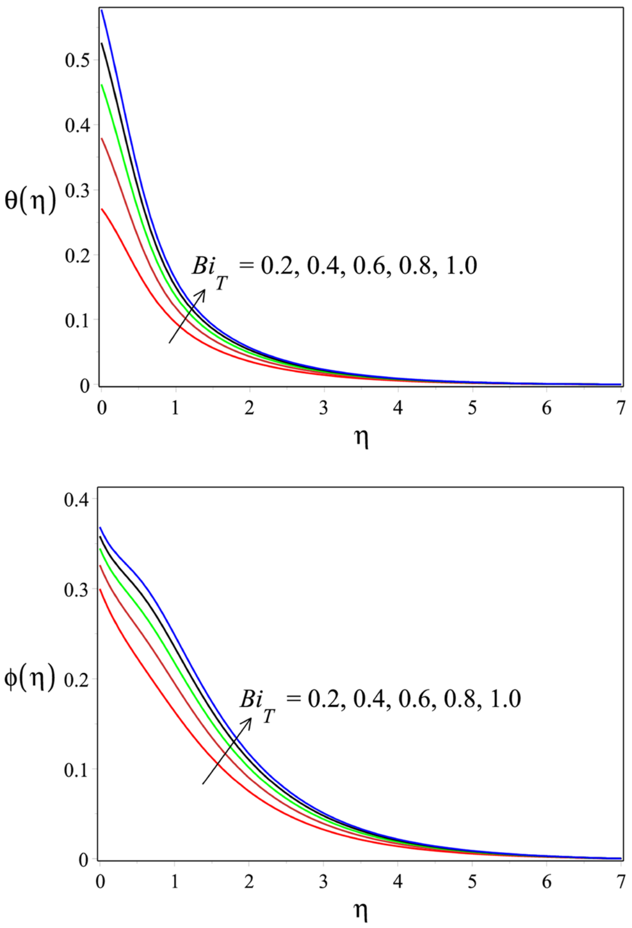

Figure 5: Temperature and concentration profiles for different values of Bi_T with Pr = 6.7, Sc = 1, Fr = 0.2, E = 0.5, n = 0.5, β = 0.5, σ = 0.5, λ = 0.2, Bi_C = 0.3, Hg = 0.1, δ = 0.5, Nb = 0.3, Nt = 0.1, Sr = 0.2, Df = 0.2 and Rd = 0.5.

$$u\frac{\partial C}{\partial x}+v\frac{\partial C}{\partial y}+w\frac{\partial C}{\partial z} = D_{\mathrm{m}}\frac{\partial^2 c}{\partial z^2} + \frac{D_{\mathrm{T}}}{T_\infty}\left(\frac{\partial^2 T}{\partial z^2}\right) - K_{\mathrm{r}}^2\left(\frac{T}{T_\infty}\right)^n e^{\frac{-E_a}{\kappa T}}(C-C_\infty) + \frac{D_{\mathrm{m}}k_{\mathrm{T}}}{T_{\mathrm{m}}}\frac{\partial^2 T}{\partial Z^2}. \quad (5)$$

The solute diffusivity (D_{m}), porous medium permeability (K_{p}), thermal diffusivity (α_{m}), kinematic viscosity (ν), density (ρ), specific heat (c_{p}), drag co-efficient (C_{b}), and non-uniform inertia co-efficient $\left[F=\left(\frac{C_{\mathrm{b}}}{K^{1/2}}\right)\right]$ are physical quantities in the above-mentioned model. The term $K_{\mathrm{r}}^2\left(\frac{T}{T_\infty}\right)^n e^{\frac{-E_{\mathrm{a}}}{\kappa T}}(C-C_\infty)$ denotes the Arrhenius function with AE (E_{a}), CR rate constant (K_{r}^2), Boltzmann constant ($\kappa = 8.61\times10^{-5}$ eV/K), and fitted rate constant (n).

The heat flux due to thermal radiation, based on the Rosseland approximation, is defined as

$$q_{\mathrm{r}} = -\frac{4\sigma^*}{3k^\#}\frac{\partial T^4}{\partial y}$$

where $k^\#$ & σ^* stand for the mean absorption coefficient and the Stefan–Boltzmann constant, respectively. It is acknowledged that the temperature differential within the stream is too tiny to allow T^4 to be expressed by Taylor's series. Extending T^4 about T_∞ and ignoring higher level terms, we can then find $T^4 \cong 4TT_\infty^3 - 3T_\infty^4$. Then, substitute this into Eq. (5) to obtain the energy equation.

The values at the boundary are

$$u = ax,\quad v = 0,\quad w = 0,\quad -k\frac{\partial T}{\partial z} = h_{\mathrm{T}}(T_{\mathrm{w}}-T),$$
$$-D_{\mathrm{m}}\frac{\partial C}{\partial z} = h_{\mathrm{c}}(C_{\mathrm{W}}-C)\ \text{when}\ z=0$$
$$u\to0,\quad v\to0,\quad T\to T_\infty,\quad C\to C_\infty\ \text{as}\ z\to\infty. \quad (6)$$

Here, T_∞ and C_∞ are ambient (free stream) temperature and concentration, respectively.

The subsequent variables are presented to transform the governing model.

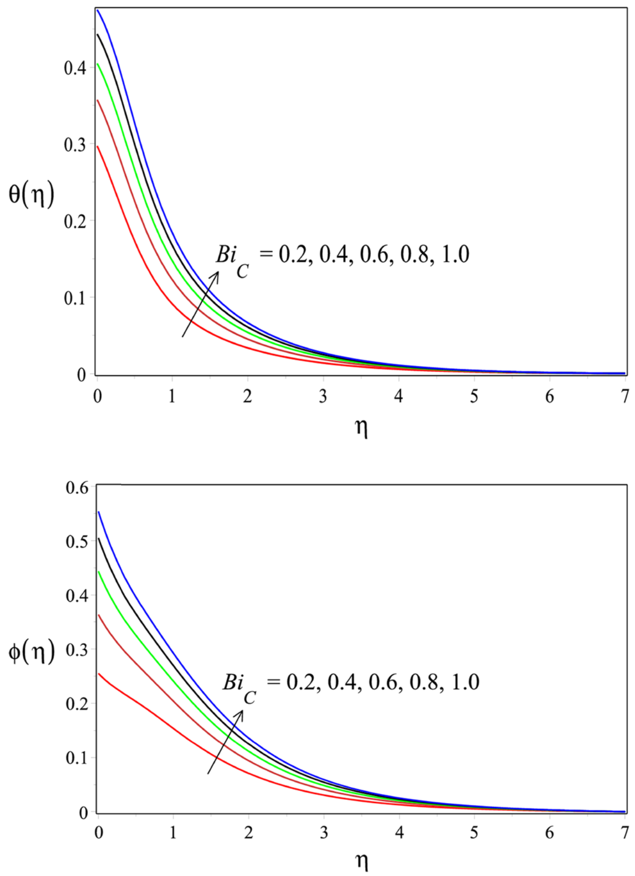

Figure 6: Temperature and concentration profiles for different values of $\mathrm{Bi_C}$ with Pr = 6.7, Sc = 1, Fr = 0.2, E = 0.5, n = 0.5, β = 0.5, σ = 0.5, $\mathrm{Bi_T}$ = 0.3, λ = 0.2, Hg = 0.1, δ = 0.5, Nb = 0.3, Nt = 0.1, Sr = 0.2, Df = 0.2 and Rd = 0.5.

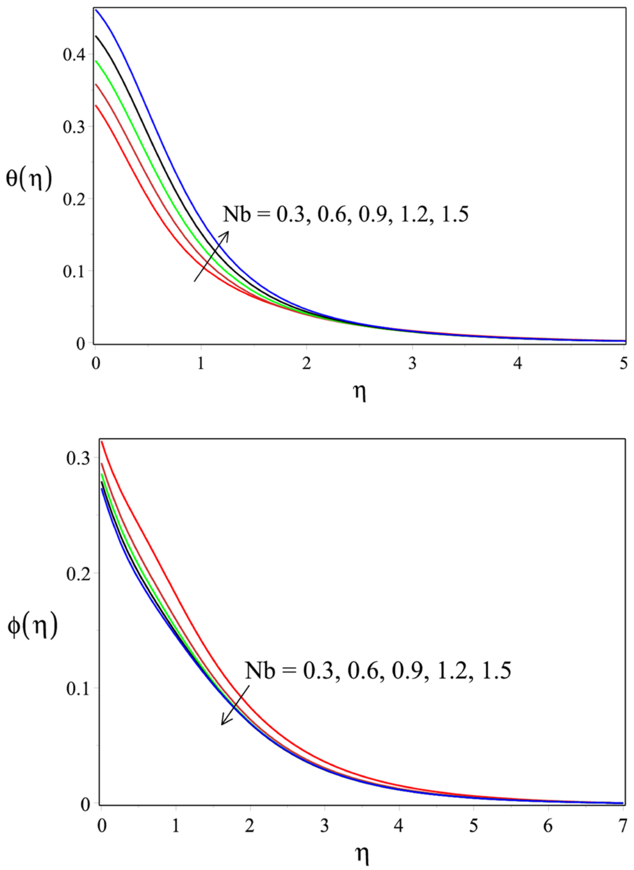

Figure 7: Temperature and concentration profiles for different values of Nb with Pr = 6.7, Sc = 1, Fr = 0.2, E = 0.5, n = 0.5, β = 0.5, σ = 0.5, $\mathrm{Bi_T}$ = 0.3, $\mathrm{Bi_C}$ = 0.3, Hg = 0.1, δ = 0.5, λ = 0.2, Nt = 0.1, Sr = 0.2, Df = 0.2 and Rd = 0.5.

$$\eta = z\sqrt{\frac{a}{\upsilon}}, \quad u = axf'(\eta), \quad v = axg(\eta),$$
$$w = -(a\upsilon)^{\frac{1}{2}}f(\eta), \tag{7}$$
$$\theta(\eta) = \frac{T - T_\infty}{T_\mathrm{W} - T_\infty}, \phi(\eta) = \frac{C - C_\infty}{C_\mathrm{W} - C_\infty}.$$

The continuity Eq. (1) is usually satisfied. The model (2–6) becomes

$$f''' + ff'' - \lambda f' + 2\beta g - (1 + F_\mathrm{r})f'^2 = 0, \tag{8}$$

$$g'' + fg' - f'g - 2\beta f' - \lambda g - F_\mathrm{r}g^2 = 0, \tag{9}$$

$$\left(\frac{1}{P_\mathrm{r}}\right)\left(1 + \frac{4}{3}\mathrm{Rd}\right)\theta'' + f\theta' + N_\mathrm{b}\theta'\phi' + N_\mathrm{t}\theta'^2 + \mathrm{Hg}\theta + \mathrm{Df}\phi'' = 0, \tag{10}$$

$$\frac{1}{S_\mathrm{c}}\phi'' + f\phi' + \frac{N_\mathrm{t}}{N_\mathrm{b}}\theta'' - \sigma[1 + \delta\theta]^n\mathrm{Exp}\left(-\frac{E}{1 + \delta\theta}\right)\phi + \mathrm{Sr}\theta'' = 0. \tag{11}$$

The valid constrains at surface are:

$$f = 0.0, \quad f' = 1.0, \quad g = 0.0, \quad \theta' = -\mathrm{Bi_T}(1 - \theta),$$
$$\phi' = -\mathrm{Bi_c}(1 - \phi) \text{ at } \eta = 0$$
$$f' \to 0.0, \quad g \to 0.0, \phi \to 0.0, \theta \to 0.0, \quad \text{as } \eta \to \infty, \tag{12}$$

where $E = \frac{E_\mathrm{a}}{\kappa T_\infty}$ is the activation energy, $\mathrm{Hg} = \frac{\mathrm{Q}}{\mathrm{a}\rho c_\mathrm{p}}$ is the heat generation parameter, $F_\mathrm{r} = \left(\frac{C_\mathrm{b}}{K^{1/2}}\right)$ is inertia coefficient, $\mathrm{Pr} = \frac{\nu}{\alpha}$ is the Prandtl number, $\mathrm{Rd} = \frac{4\sigma^* \; T_\infty^3}{kk^\#}$ is the parameter for radiation, $\beta = \frac{\Omega}{a}$ is the rotational parameter, $\lambda = \frac{\nu}{K_\mathrm{p}a}$ represents the permeability parameter, $\mathrm{Sc} = \frac{\nu}{D_\mathrm{m}}$ is the Schmidt number, $\mathrm{Df} = \frac{D_\mathrm{m}k_\mathrm{T}(C_\mathrm{W} - C_\infty)}{C_\mathrm{s}C_\mathrm{p}(T_\mathrm{W} - T_\infty)\upsilon}$ is the Dufour number, $\mathrm{Sr} = \frac{D_\mathrm{m}k_\mathrm{T}(T_\mathrm{W} - T_\infty)}{T_\mathrm{m}\upsilon(C_\mathrm{W} - C_\infty)}$ is the Soret number, $\delta = \frac{T_\mathrm{W} - T_\infty}{T_\infty}$ is a parameter for temperature difference, and $\sigma = \frac{K_\mathrm{r}^2}{a}$ is the dimensionless reaction rate.

The Nusselt number (Nu) indicates the amount of heat transferred through a fluid as a result of convection. The

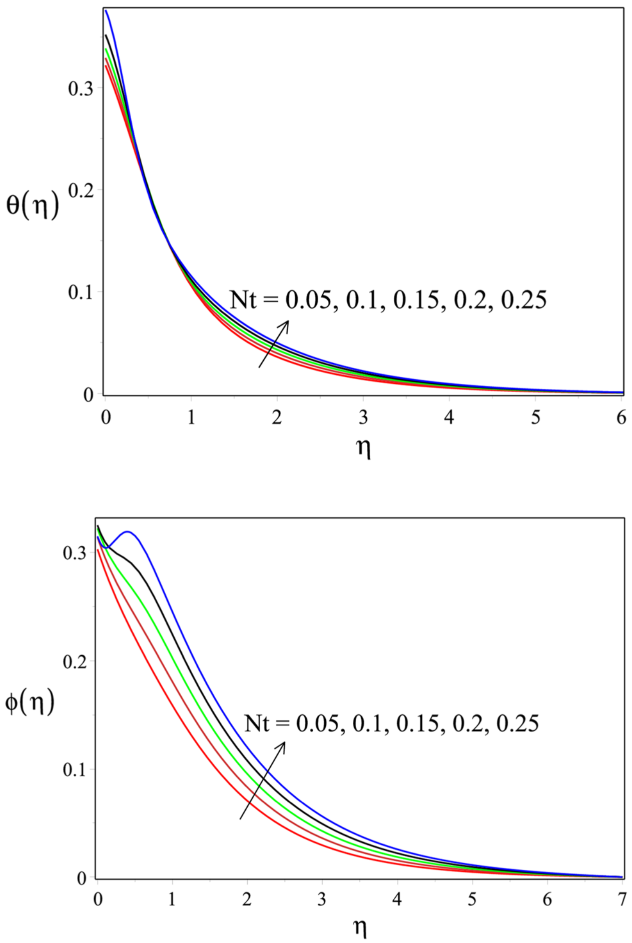

Figure 8: Temperature and concentration profiles for different values of Nt with Pr = 6.7, Sc = 1, Fr = 0.2, E = 0.5, n = 0.5, β = 0.5, σ = 0.5, $\mathrm{Bi_T}$ = 0.3, $\mathrm{Bi_C}$ = 0.3, Hg = 0.1, δ = 0.5, Nb = 0.3, λ = 0.2, Sr = 0.2, Df = 0.2 and Rd = 0.5.

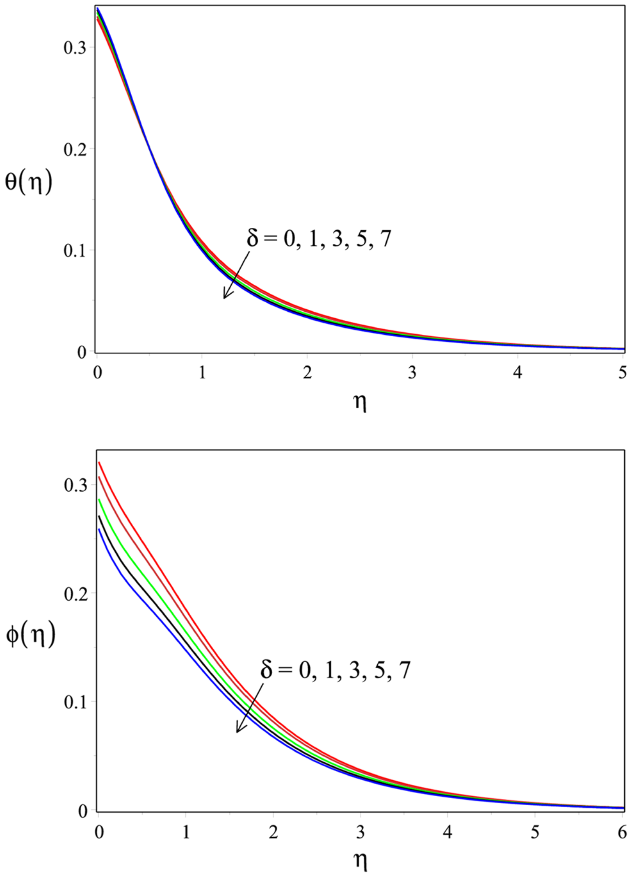

Figure 9: Temperature and concentration profiles for different values of δ with Pr = 6.7, Sc = 1, Fr = 0.2, E = 0.5, n = 0.5, β = 0.5, σ = 0.5, $\mathrm{Bi_T}$ = 0.3, $\mathrm{Bi_C}$ = 0.3, Hg = 0.1, λ = 0.2, Nb = 0.3, Nt = 0.1, Sr = 0.2, Df = 0.2 and Rd = 0.5.

Sherwood number (Sh) indicates the rate of solute mass transfer across the system. The skin friction (Cf) factor derives the rate of frictional (drag) force along the surface. All the quantities are defined as follows:

The quantity of heat transfer is indicated by the Nusselt number, $\mathrm{Nu}_x = \frac{x q_\mathrm{w}}{k(T_\mathrm{w} - T_\infty)}$ with $q_\mathrm{w} = -k_\mathrm{T}\frac{\partial T}{\partial z}\big|_{z=0}$. The solute transfer across the system is indicated by the Sherwood number, $\mathrm{Sh}_x = \frac{x j_\mathrm{w}}{D(C_\mathrm{w} - C_\infty)}$ with $j_\mathrm{w} = -D\frac{\partial C}{\partial z}\big|_{z=0}$. The rate of frictional (drag) force along the surface is determined by the skin friction factor, $C_\mathrm{f} = \frac{VF_\mathrm{w}}{\rho U_\mathrm{w}^2}$ with $VF_\mathrm{w} = \mu\left(\frac{\partial u}{\partial z}\right)$. Finally, we have the dimensionless form of physical quantities:

$$C_\mathrm{f}\sqrt{\mathrm{Re}_x} = f''(0), \quad \frac{\mathrm{Nu}_x}{\sqrt{\mathrm{Re}_x}} = -\left(1 + \frac{4}{3}\mathrm{Rd}\right)\theta'(0), \quad \frac{\mathrm{Sh}_x}{\sqrt{\mathrm{Re}_x}} = -\phi'(0), \tag{13}$$

where $\mathrm{Re}_x = \frac{U_0 x}{\nu}$ denotes local Reynolds number.

3 Method of solution

The solutions of the governing model are needed to understand the physical phenomena clearly for predicting and controlling numerous engineered systems. The governing model of equations is quite difficult to solve due to the possibility of extremely chaotic behaviour in the solution. The closed form of solutions cannot be established because of the nonlinear nature of the system of equations. As such, we want to find a numerical solution for the governing model. Using the shooting approach, the Runge–Kutta method is implemented to solve the equations. Since a crucial component of the numerical solution is compared with the numerical values, the current computational code is compared to the previous findings, as found by Rashid *et al.* [45]. It is displayed in Table 1. It is detected that the present results agree well with the existing data, and it gives confidence in our calculations.

4 Results and discussion

The three-dimensional doubly diffusive convective rotating nanoliquid stream in a Darcy–Forchheimer porous medium

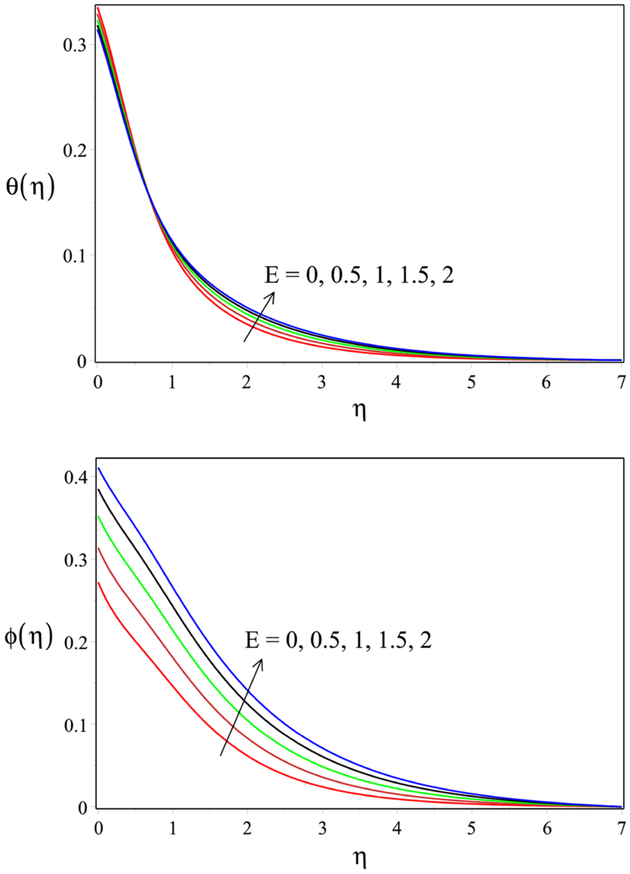

Figure 10: Temperature and concentration profiles for different values of E with Pr = 6.7, Sc = 1, Fr = 0.2, λ = 0.2, n = 0.5, β = 0.5, σ =0.5, $\mathrm{Bi_T}$ = 0.3, $\mathrm{Bi_C}$ = 0.3, Hg = 0.1, δ = 0.5, Nb = 0.3, Nt = 0.1, Sr = 0.2, Df = 0.2 and Rd = 0.5.

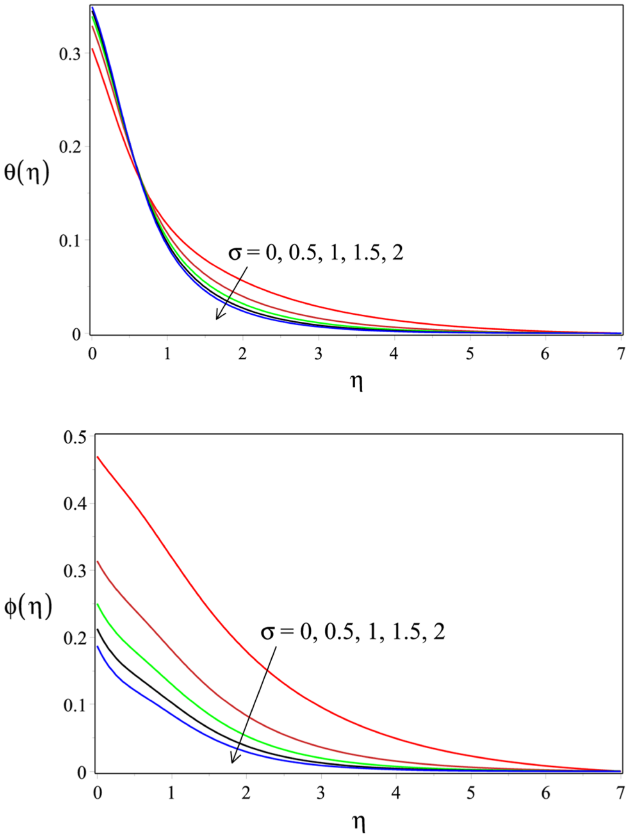

Figure 11: Temperature and concentration profiles for different values of σ with Fr = 0.2, E = 0.5, n = 0.5, β = 0.5, λ = 0.2, $\mathrm{Bi_T}$ = 0.3, $\mathrm{Bi_C}$ = 0.3, Hg = 0.1, δ = 0.5, Nb = 0.3, Nt = 0.1, Sr = 0.2, Df = 0.2 and Rd = 0.5.

under the influence of AE, thermal radiation, Dufour and Soret effects is explored numerically under various groupings of appropriate parameters involved herein. The values of the parameter fall into the following range with Pr = 6.7 and Sc = 1. The rotational parameter (β) varies ($0 \le \beta \le 2$), radiation parameter (Rd) varies($0 \le \beta \le 2$), inertia parameter (Fr) varies ($0 \le \mathrm{Fr} \le 1.5$), Soret number (Sr) varies ($0 \le \mathrm{Sr} \le 0.8$), the Dufour number (Df) varies ($0 \le \mathrm{Df} \le 0.5$), permeability parameter (λ) ranges from 0 to 8, AE parameter (E) varies ($0 \le E \le 3$), thermal Biot number ($\mathrm{Bi_T}$) and solutal Biot number ($\mathrm{Bi_c}$) take values from 0 to 1, heat generation/absorption (Hg) takes values ($-0.5 \le \mathrm{Hg} \le 0.5$), Brownian motion parameter ($0 \le \mathrm{Nb} \le 1.5$), thermophoresis parameter ($0 \le \mathrm{Nt} \le 0.3$), ($-1 \le n \le +1$), reaction rate takes values ($0 \le \sigma \le 2$), and parameter for temperature difference takes values ($0 \le \delta \le 7$).

The effect of the rotational parameter on stream, thermal, and solutal fields is shown in Figure 2(a) and (c). It is evident that the rotational parameter values are strengthened by the stream speed. In other words, the fluid velocity is suppressed by the strength of the rotation. Conversely, the thermal field is supported by the rotational strength, that is, when "β" increases, the temperature also rises within the boundary layer regime. Unlike thermal fields, solutal field is unaffected. Nonetheless, "β" has a very noticeable effect on concentration. As the rotational strength grows, so does the solute concentration, see Figure 2(c). The impact of the inertia parameter on temperature, concentration, and velocity is depicted in Figure 3(a)–(c). Temperature, velocity, and solute distributions have little effect on altering Fr values.

The determination of permeability parameter (λ) on a stream, thermal, and solutal fields is depicted in Figure 4(a)–(c). Permeability has a very strong impact on fluid flow and thermal and solutal distributions inside the boundary layer regime. As the permeability parameter values increase, the velocity of the fluid particles declines. Conversely, temperature and concentration rises with increasing permeability parameter values. The permeability of the porous matrix decreases, resulting in a slowdown of the stream flow rate. However, the porous structure enhances the thermal exchange and increases the temperatures inside the boundary layer. The concentration exhibits a peculiar effect with permeability parameter. The solute concentration declines near the boundary and it

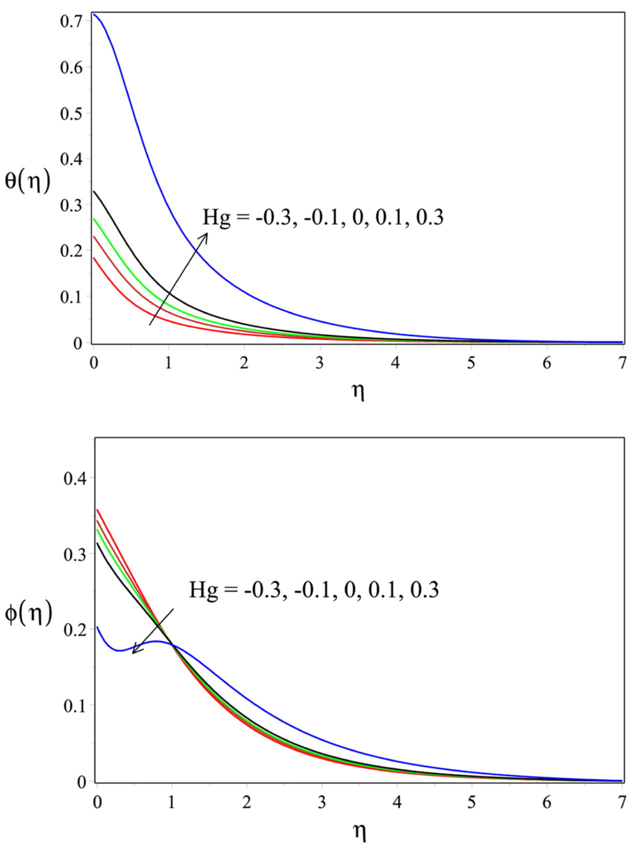

Figure 12: Temperature and concentration profiles for different values of Hg with Fr = 0.2, E = 0.5, n = 0.5, β = 0.5, σ = 0.5, $\mathrm{Bi_T}$ = 0.3, $\mathrm{Bi_C}$ = 0.3, λ = 0.2, δ = 0.5, Nb = 0.3, Nt = 0.1, Sr = 0.2, Df = 0.2 and Rd = 0.5.

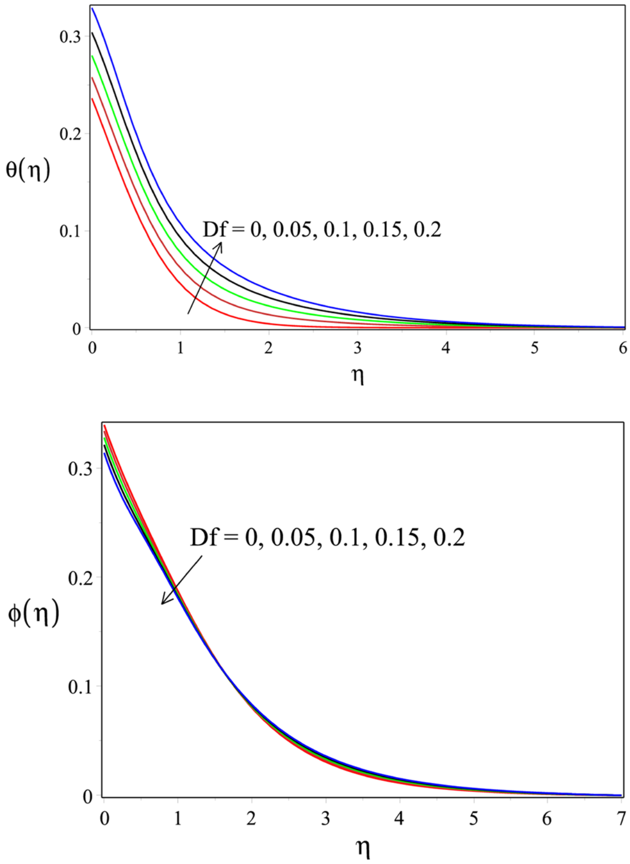

Figure 13: Temperature and concentration profiles for different values of Df with Fr = 0.2, E = 0.5, n = 0.5, β = 0.5, σ = 0.5, $\mathrm{Bi_T}$ = 0.3, $\mathrm{Bi_C}$ = 0.3, Hg = 0.1, δ = 0.5, Nb = 0.3, Nt = 0.1, Sr = 0.2, λ = 0.2, and Rd = 0.5.

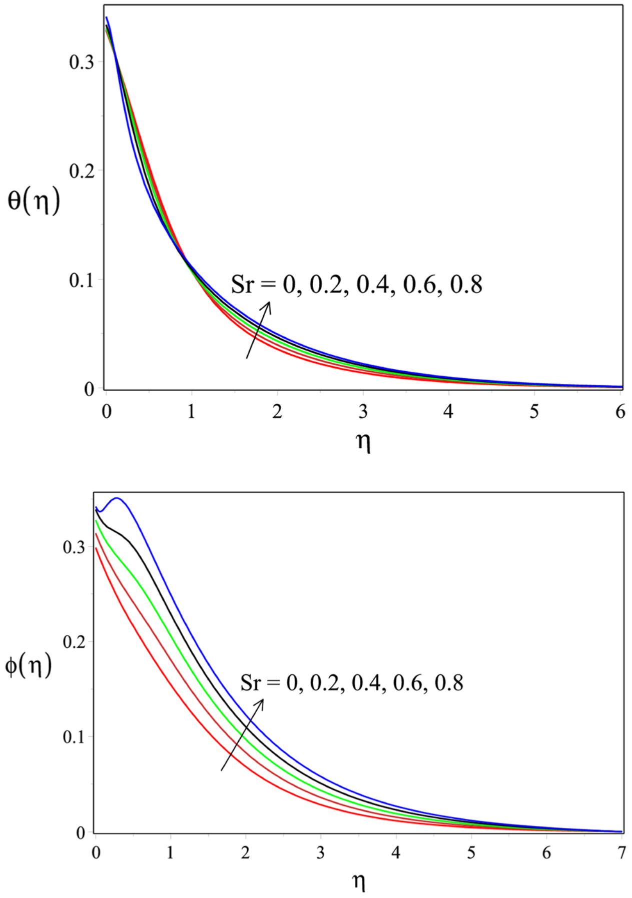

Figure 14: Temperature and concentration profiles for different values of Sr with Fr = 0.2, E = 0.5, n = 0.5, β = 0.5, σ = 0.5, $\mathrm{Bi_T}$ = 0.3, $\mathrm{Bi_C}$ = 0.3, Hg = 0.1, δ = 0.5, Nb = 0.3, Nt = 0.1, λ = 0.2, Df = 0.2 and Rd = 0.5.

enhances slightly away from boundary, which is clearly seen from Figure 4(c). Figure 5(a) and (b) presents the outcome of thermal Biot number on solute and temperature profiles. The thermal Biot number supports the thermal and solutal fields.

Figure 6(a) and (b) shows the influence of solutal Biot number on thermal and solutal distributions with $\beta = E = \sigma = \delta = n = \mathrm{Rd} = 0.5$, $\mathrm{Bi_T} = \mathrm{Nb} = 0.3$, $\lambda = \mathrm{Fr} = 0.2$, $\mathrm{Nb} = 0.3$, $\mathrm{Nt} = \mathrm{Hg} = 0.1$, $\mathrm{Sr} = \mathrm{Df} = 0.2$. Both thermal and solute concentration improve when rising the values of $\mathrm{Bi_C}$. Both Biot numbers ($\mathrm{Bi_T}$ and $\mathrm{Bi_C}$) provide a remarkable impact on thermal and concentration fields. Figure 7(a) and (b) examines how temperature and concentration are affected by the Brownian motion parameter with $\mathrm{Rd} = 0.5$, $\mathrm{Hg} = \mathrm{Nt} = 0.1$, $\mathrm{Bi_T} = \mathrm{Bi_c} = 0.3$, $\mathrm{Fr} = 0.2$, $E = n = \beta = \delta = \sigma = 0.5$, and $\lambda = \mathrm{Sr} = \mathrm{Df} = 0.2$. The Brownian motion parameter shows a strong impact on the thermal field compared to that on the solute field, which is clearly indicated in Figure 7(a) and (b). It is also found that concentration and temperature exhibit opposite trends when rising the values of Nb. That is, temperature enhances and

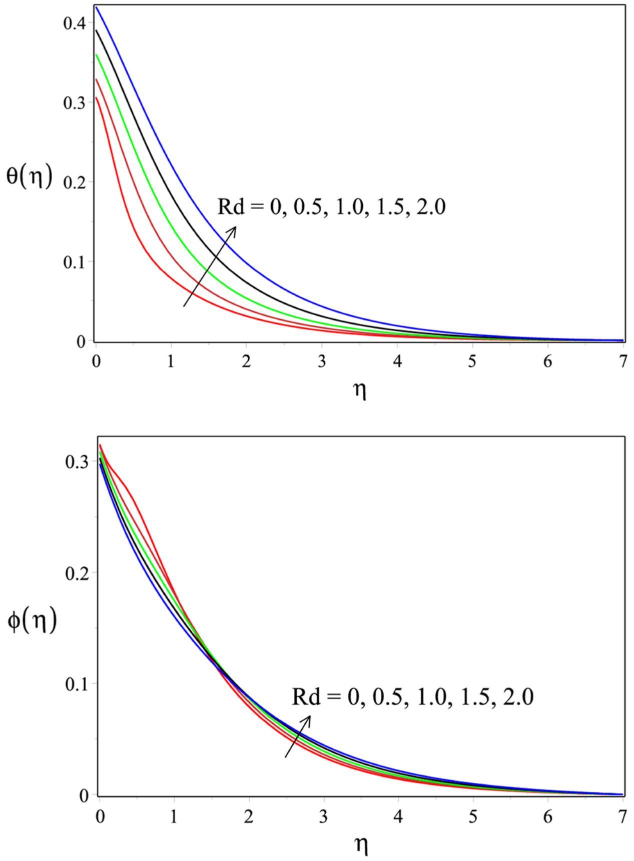

Figure 15: Temperature and concentration profiles for different values of Sr with Pr = 6.7, Sc = 1, Fr = 0.2, E = 0.5, n = 0.5, β = 0.5, σ = 0.5, $\mathrm{Bi_T}$ = 0.3, $\mathrm{Bi_C}$ = 0.3, Hg = 0.1, δ = 0.5, Nb = 0.3, Nt = 0.1, λ = 0.2, Df = 0.2 and Sr = 0.2.

Table 2: The values of $-f''(0), -g''(0), -\theta'(0), -\phi'(0)$ for different Fr, λ, β with Pr = 6.7, Sc = 1, E = 0.5, n = 0.5, Hg = 0.1, σ = 0.5, δ = 0.5, Nb = 0.3, Nt = 0.1, $\mathrm{Bi_T}$ = 0.3 and $\mathrm{Bi_C}$ = 0.3, Sr = 0.2, Df = 0.2, and Rd = 0.5

β	λ	Fr	$-f''(0)$	$-g''(0)$	$-\theta'(0)$	$-\phi'(0)$
0.5	0.2	0	1.204477	0.475714	0.336305	0.205792
		0.3	1.280899	0.471634	0.333471	0.205783
		0.6	1.353549	0.468108	0.330684	0.205801
		0.9	1.422922	0.465086	0.327930	0.205843
		1.2	1.489417	0.462529	0.325197	0.205907
0.5	0	0.1	1.165652	0.511399	0.337307	0.205794
	2		1.777592	0.300514	0.305744	0.206822
	4		2.262783	0.229805	0.263653	0.210838
	6		2.665351	0.192876	0.211285	0.217454
	8		3.015861	0.169391	0.140251	0.227257
0.1	0.2	0.1	1.130227	0.107794	0.346602	0.206393
0.5			1.230406	0.474289	0.335355	0.205786
1.0			1.396760	0.799684	0.311040	0.206397
1.5			1.557034	1.048763	0.166838	0.209216
2.0			1.705806	1.255849	0.233619	0.214453

solute concentration declines on rising the values of Nb. Figure 8(a) and (b) illustrates the influence of thermophoresis parameter (Nt) on solute concentration and temperature fields with $n = E = \delta = \beta = \sigma = 0.5$, $\mathrm{Nb} = \mathrm{Bi_T} = \mathrm{Bi_c} = 0.3$, $\mathrm{Hg} = 0.1$, $\mathrm{Fr} = \lambda = \mathrm{Sr} = \mathrm{Df} = 0.2$, and $\mathrm{Rd} = 0.5$. Comparing both figures, it is understood that thermophoresis parameter has a greater impact on the solute profile at higher values of Nt. There is an overshoot of the solute profile as the values of Nt continue to rise. The solute concentration enriches when the values of Nt are raised. On the contrary, there is no considerable effect on the temperature profile on changing the values of Nt.

Figure 9(a) and (b) shows the impact of "δ" on the profile of θ and ϕ for $E = n = \beta = \mathrm{Rd} = \sigma = 0.5$, $\mathrm{Bi_T} = \mathrm{Bi_C} = 0.3$, $\mathrm{Sr} = \mathrm{Df} = 0.5$, $\lambda = 0.2$. Both temperature and solute decline as the values of "δ" increase. The influence of AE parameter (E) on thermal and solutal distribution is illustrated in Figure 10(a) and (b) for $\sigma = n = \beta = \mathrm{Rd} = \delta = 0.5$, $r = \lambda = 0.2$, $\mathrm{Sr} = \mathrm{Df} = 0.5$. The impact of AE is more pronounced on solutal transport than that on thermal transport because the parameter "E" is directly involved in the solute transport equation. The solute profile enhances with an increase in the AE parameter values. A slight increase in temperature is observed as the value of E rises. The influence of σ on temperature and concentration is clearly seen in Figure 11(a) and (b) with $\mathrm{Fr} = 0.2$, $\beta = n = \delta = E = 0.5$, $\lambda = \mathrm{Sr} = \mathrm{Df} = 0.2$, $\mathrm{Bi_T} = \mathrm{Bi_C} = 0.3$, $\mathrm{Hg} = 0.1$, $\mathrm{Nt} = 0.1$, $\mathrm{Nb} = 0.3$, and $\mathrm{Rd} = 0.5$. The solute transport shows more variation as the "σ" values increase. That is, the solutal distribution declines with increasing "σ" values and and a corresponding decrease in temperature is also observed.

Figure 12(a) and (b) provides the internal heat generation (Hg) effects on the fields of temperature and solutal concentration. It is evidently seen that the internal heat generation boosts up the temperature within the system, resulting in an increase in thermal profiles. The concentration gets less important with Hg. The power of Dufour parameter on thermal and solutal fields is displayed in Figure 13(a) and (b)

Table 3: The values of $-\theta'(0)$, $-\phi'(0)$ for different $\mathrm{Bi_T}$, $\mathrm{Bi_C}$, Hg, Nb, Nt, δ, with Pr = 6.7, Sc = 1, $E = \beta = \sigma = \mathrm{Rd} = 0.5 = 0.5$, Fr = 0.1, $\mathrm{Sr} = \mathrm{Df} = \lambda = 0.2$

$\mathrm{Bi_T}$	$\mathrm{Bi_C}$	Hg	Nb	Nt	δ	$-\theta'(0)$	$-\phi'(0)$
0.2	0.3	0.1	0.3	0.1	0.5	0.243035	0.210134
0.4						0.413465	0.202193
0.6						0.537708	0.196643
0.8						0.631512	0.192591
1.0						0.704487	0.189521
0.3	0.2	0.1	0.3	0.1	0.5	0.351398	0.148919
	0.4					0.321256	0.254505
	0.6					0.297576	0.333859
	0.8					0.278413	0.395951
	1.0					0.262552	0.445999
0.3	0.3	−0.3	0.3	0.1	0.5	0.407816	0.192543
		−0.1				0.384430	0.196894
		0				0.219174	0.200394
		0.1				0.335355	0.205786
		0.3				0.142731	0.238931
0.3	0.3	0.1	0.2	0.1	0.5	0.339441	0.201141
			0.3			0.335355	0.205786
			0.4			0.330685	0.208393
			0.5			0.325777	0.210133
			0.6			0.320696	0.211435
0.3	0.3	0.1	0.6	0.05	0.5	0.338976	0.209111
				0.1		0.335355	0.205786
				0.15		0.330688	0.203315
				0.2		0.323950	0.202437
				0.25		0.311836	0.205519
0.3	0.3	0.1	0.3	0.1	0	0.336025	0.203649
					1	0.334754	0.207716
					3	0.332848	0.213927
					5	0.331457	0.218547
					7	0.330373	0.222190

Table 4: The values of $-\theta'(0)$, $-\phi'(0)$ for different E, n, σ , Sr, Df, Rd with Pr = 6.7, Sc = 1, $\mathrm{Nb} = \mathrm{Bi_T}, = \mathrm{Bi_C} = 0.3$, $\delta = \beta = 0.5$, Hg = Nt = Fr = 0.1, $\lambda = 0.2$

E	n	σ	Sr	Df	Rd	$-\theta'(0)$	$-\phi'(0)$
0	0.5	0.5	0.2	0.2	0.5	0.332157	0.218286
0.5						0.335354	0.205786
1						0.338301	0.194266
1.5						0.340821	0.184439
2						0.342823	0.176666
0.5	−0.8	0.5	0.2	0.2	0.5	0.336242	0.202960
	−0.4					0.335978	0.203807
	0					0.335706	0.204674
	0.4					0.335426	0.205561
	0.8					0.335138	0.206469
0.5	0.5	0	0.2	0.2	0.5	0.347389	0.159128
		0.5				0.335355	0.205785
		1				0.330323	0.224934
		1.5				0.327299	0.236180
		2				0.325203	0.243796
0.5	0.5	0.5	0	0.2	0.5	0.335663	0.210311
			0.2			0.335355	0.205786
			0.4			0.334644	0.201621
			0.6			0.333087	0.198284
			0.8			0.329345	0.197348
0.5	0.5	0.5	0.2	0	0.5	0.381842	0.198111
				0.05		0.371083	0.199803
				0.10		0.359849	0.201618
				0.15		0.348006	0.203593
				0.20		0.335355	0.205786
0.5	0.5	0.5	0.2	0.2	0	0.208083	0.205494
					0.5	0.335354	0.205786
					1	0.447717	0.207472
					1.5	0.182732	0.209158
					2	0.637848	0.210732

with Fr = 0.2, $\beta = \delta = E = \sigma = n = 0.5$, $\sigma = 0.5$, $\mathrm{Bi_T} = \mathrm{Bi_C} = 0.3$, Hg = 0.1, Nt = 0.1, Sr = λ = 0.2, Nb = 0.3, and Rd = 0.5. Figure 13(a) shows the Dufour number yields more impression on thermal field. That is, the temperature of the system increases with the increase in the Dufour parameter. On the other side, an inconsiderable impact is found on solutal distribution with Df. Figure 14(a) and (b) provides the outcome of the Soret parameter on θ and ϕ, with λ = Fr = Df = 0.2, $\beta = n = \sigma = E = \delta = 0.5$, $\mathrm{Bi_T} = \mathrm{Bi_C} = 0.3$, Hg = 0.1, $\delta = 0.5$, Nb = 0.3, Nt = 0.1, and Rd = 0.5. The solute distribution enhances with Soret number. An overshoot is detected near the boundary for higher values of Sr. No noteworthy fact on temperature is discovered on changing the Sr values. Figure 15(a) and (b) provides the consequences of thermal radiation on θ and ϕ. The radiation parameter strongly influences the thermal field which is clearly seen from the temperature profiles in Figure 15(a). The temperature increases significantly with increasing thermal radiation values. However, no notable impact on ϕ is observed with Rd values.

Table 2 provides the impact of $-f''(0)$, $-g''(0)$, $-\theta'(0)$, $-\phi'(0)$ values with different combinations of pertinent parameters involved in the study. The skin friction $(-f''(0))$ increases with increasing the values of Fr, λ, β. $-g''(0)$ declines with increasing the values of Fr, λ and it rises on strengthening "β" values. The local heat energy transport suppresses on strengthening the values of the inertia parameter (Fr), permeability parameter (λ), and rotational parameter (β). The rate of local solute transfer diminishes with increasing the values of λ. Tables 3 and 4 demonstrate the consequences of local heat and mass transfer rate under several groupings of appropriate parameters presented in the research. Both Biot numbers have opposite behaviours to local heat/mass transport rates. That is, the heat (mass) transport enhances (declines) with increasing the thermal Biot number. On the contrary, the local heat (solute) transfer suppresses (augments) on strengthening the solutal Biot number. The AE parameter supports local energy transfer and it suppress local mass transport. The Brownian motion of the particle boosted-up the local mass transport within the system. With increasing the value of Df and Sr, the local heat transfer rate decreases. The local heat energy transfer decreases with higher values of Hg, Nb, Nt, n, and Rd. The local mass transfer augments as the values of n, Sr, Rd, Hg increase. However, the value of $-\phi'(0)$ decreases with increasing the Nt and Df values.

5 Conclusion

The influence of AE, thermal radiation, cross diffusion (Dufour & Soret) effects on three-dimensional doubly diffusive convective rotating nanoliquid stream in a Darcy–Forchheimer porous medium is discovered numerically under several groupings of parameters involved. The following are deduced from the study.

- The strength of the rotation suppresses the fluid velocity while supports the thermal and solutal fields.
- The temperature enhances largely on rising the thermal radiation, Dufour values.
- The AE is more pronounced on solutal transport than that of on thermal transport.
- The skin friction $(-f'')$ rises on increasing the values of Fr, λ, β. The skin friction $(-g'')$ deteriorates by rising the values of Fr, λ and it rises on strengthening "β" values.
- The local heat transfer drops on raising the values of Hg, Nb, Nt, n and Rd values.
- The both Biot numbers makes opposite behaviour on local heat & mass transport rate.
- The local solute transfer augments when increasing the n, Sr, Rd, & Hg values.
- The rate of heat transport suppresses on strengthening the values of inertia parameter, permeability parameter, and rotational parameter.
- The results may applicable to the thermal systems involving cooling of electronic equipment, food processing, paper and sheet production.

Funding information: The authors state no funding involved.

Author contributions: Conception and design: SS, material preparation: SS and TJA, data collection and analysis: SS, software: SS. Draft of the manuscript: SS and TJA, review and editing: SS and HMA. All authors have accepted responsibility for the entire content of this manuscript and approved its submission.

Conflict of interest: The authors state no conflict of interest.

Data availability statement: The datasets generated and/or analysed during the current study are available from the corresponding author on reasonable request.

References

[1] Richa, Sharma BK, Almohsen B, Laroze D. Intelligent neuro-computational modelling for MHD nanofluid flow through a curved stretching sheet with entropy optimization: Koo–Kleinstreuer–Li approach. J Comput Des Eng. 2024;11(5):164–83. doi: 10.1093/jcde/qwae078.

[2] Sharma PK, Sharma BK, Sharma M, Almohsen B, Laroze D, Saluja R. Influence of magnetohydrodynamics and chemical reactions on oscillatory free convective flow through a vertical channel in a rotating system with variable permeability. Mod Phys Lett B. 2025;39(19):2550050.

[3] Kumara Swamy HA, Sankar M, Keerthi Reddy N, Do Y. Optimization of entropy generation and thermal mechanism of MHD hybrid nanoliquid flow in a sinusoidally heated porous cylindrical chamber. Case Stud Therm Eng. 2023;51:103615.

[4] Reddy NK, Sankar M. Buoyant heat transfer of nanofluids in a vertical porous annulus: a comparative study of different models. Int J Numer Methods Heat Fluid Flow. 2023;33(2):477–509.

[5] Sivasankaran S, Mallawi FOM. Numerical study on convective flow boiling of nanoliquid inside a pipe filling with aluminum metal foam by two-phase model. Case Stud Therm Eng. 2021;26:101095 (1–14).

[6] Kumar A, Sharma BK, Muhammad T, Pérez LM. Optimization of thermal performance in hybrid nanofluids for parabolic trough solar collectors using Adams–Bashforth–Moulton method. Ain Shams Eng J. 2024;15(12):103106.

[7] Sivasankaran S, Bhuvaneswari M. Numerical study on influence of water based hybrid nanofluid and porous media on heat transfer and pressure loss. Case Stud Therm Eng. 2022;34:102022.

[8] Abdul Hakeem AK, Priya S, Bhose G, Sivanandam S. Magneto-convective hybrid nanofluid slip flow over a moving inclined thin needle in a Darcy-Forchheimer porous medium with viscous dissipation. Int J Numer Methods Heat Fluid Flow. 2024;34(1):334–52.

[9] Yasmin H, Bossly R, Alduais FS, Al-Bossly A, Saeed A. Water-based hybrid nanofluid flow containing CNT nanoparticles over an extending surface with velocity slips, thermal convective, and zero-mass flux conditions. Open Phys. 2025;23(1):20250122.

[10] Noor S, Alshehry AS. Mononuclear nanofluids undergoing convective heating across a stretching sheet and undergoing MHD flow in three dimensions: Potential industrial applications. Open Phys. 2024;22:20230170.

[11] Mandal G, Pal D. Mixed convective-quadratic radiative MoS2–SiO2/H_2O hybrid nanofluid flow over an exponentially shrinking permeable Riga surface with slip velocity and convective boundary conditions: Entropy and stability analysis. Numer Heat Transfer, Part A: Appl. 2023;85(14):2315–40. doi: 10.1080/10407782.2023.2221004.

[12] Gireesha BJ, Archana M, Mahanthesh B, Prasannakumara BC. Exploration of activation energy and binary chemical reaction effects on nano Casson fluid flow with thermal and exponential space-based heat source. Multidiscip Model Mater Struct. 2019;15(1):227–45.

[13] Vinodh SR, Jagan K, Sivasankaran S. Impacts of Casson model on hybrid nanofluid flow over a moving thin needle with Dufour and Soret and thermal radiation effects. Math Comput Appl. 2022;28(1):2.

[14] Acharya N, Das K. Three-dimensional rotating flow of Cu–Al_2O_3/kerosene oil hybrid nanofluid in presence of activation energy and thermal radiation. Numer Heat Transfer Part A. 2022;84(6):586–603.

[15] Saini SK, Agrawal R, Kaswan P. Activation energy and convective heat transfer effects on the radiative Williamson nanofluid flow over a radially stretching surface containing joule heating and viscous dissipation. Numer Heat Transfer Part A. 2023;85(15):2534–57.

[16] Vijay N, Sharma K. Magnetohydrodynamic hybrid nanofluid flow over a decelerating rotating disk with Soret and Dufour effects. Multidiscip Model Mater Struct. 2023;19(2):253–76.

[17] Joyce MI, Kandasamy J, Sivanandam S. Entropy generation of Cu–Al_2O_3/water flow with convective boundary conditions through a porous stretching sheet with slip effect, Joule heating and chemical reaction. Math Comput Appl. 2023;28(1):18.

[18] Chandrapushpam T, Bhuvaneswari M, Sivanandam S. Double diffusive MHD squeezing copper water nanofluid flow between parallel plates filled with porous medium and chemical reaction. Int J Numer Methods Heat Fluid Flow. 2024;34(3):1151–69.

[19] Noor S. Homogeneous–heterogeneous reactions in the colloidal investigation of Casson fluid. Open Phys. 2024;22:20230174.

[20] Samanta A, Mondal H. Spectral quasilinearization method for Sisko nanofluid past a stretching cylinder with activation energy and entropy generation effects subject to variable thermal conductivity. Heat Transf. 2022;51(8):7773–86.

[21] Ramaiah KD, Surekha P, Kotha G, Thangavelu K. MHD rotating flow of a Maxwell fluid with Arrhenius activation energy and non-Fourier heat flux model. Heat Transf. 2020;49(4):2209–27.

[22] Bestman AR. Natural convection boundary layer with suction and mass transfer in a porous medium. Int J Eng Res. 1990;14:389–96.

[23] Huang CJ. Arrhenius activation energy effect on free convection about a permeable horizontal cylinder in porous media. Transp Porous Med. 2019;128:723–40.

[24] Kotresh MJ, Ramesh GK, Shashikala VKR, Prasannakumara BC. Assessment of Arrhenius activation energy in stretched flow of nanofluid over a rotating disc. Heat Transf. 2021;50(3):2807–28.

[25] Yesodha P, Bhuvaneswari M, Sivasankaran S, Saravanan K. Convective heat and mass transfer of chemically reacting fluids with activation energy with radiation and heat generation. J Therm Eng. 2021;7(5):1130–8.

[26] Younus M, Lakshmi AV. Numerical investigation of activation energy of radiative magnetohydrodynamic Williamson nanofluid flow. Heat Transf. 2022;51(7):6197–222.

[27] Prakash J, Bhanumathi D, Vijaya Kumar AG. Diffusion-Thermo and radiation effects on unsteady MHD flow through porous medium past an impulsively started infinite vertical plate with variable temperature and mass diffusion. Transp Porous Med. 2013;96:135–51.

[28] Chandar Rao DP, Thiagarajan S, Kumar VS. Significance of Dufour and Soret effects on the non-Darcy flow of cross fluid by a tilted plate with radiation and chemical reaction: A Cattaneo–Christov heat flux model. Heat Transf. 2022;51(2):1585–600.

[29] Sharma BR, Choudhury R, Das UJ. Soret–Dufour effects on chemically reacting non-Darcian MHD flow around a plate. Heat Transf. 2023;52(1):28–39.

[30] Haritha A, Vishali B, Venkata Lakshmi C. Heat and mass transfer of MHD Jeffrey nanofluid flow through a porous media past an inclined plate with chemical reaction, radiation, and Soret effects. Heat Transf. 2023;52(2):1178–97.

[31] Niranjan H, Sivasankaran S, Bhuvaneswari M. Chemical reaction, Soret and Dufour effects on MHD mixed convection stagnation point flow with radiation and slip condition. Sci Iran – Trans B Mech Eng. 2017;24(1):698–706.

[32] Raghunath K, Mohanaramana R. Hall, Soret, and rotational effects on unsteady MHD rotating flow of a second-grade fluid through a porous medium in the presence of chemical reaction and aligned magnetic field. Int Comm Heat Mass Trans. 2022;137:106287.

[33] Jagan K, Sivasankaran S. Soret & Dufour and triple stratification effect on MHD flow with velocity slip towards a stretching cylinder. Math Comp Appl. 2022;27(2):25.

[34] Geetha SP, Sivasankaran S, Bhuvaneswari M. Partial slip and cross-diffusion effects on Magnetohydrodynamic mixed bioconvection flow in a channel with chemical reaction. J Nanofluids. 2023;12(7):1815–26.

[35] Sharma BK, Kumar A, Almohsen B, Fernandez-Gamiz U. Computational analysis of radiative heat transfer due to rotating tube in parabolic trough solar collectors with Darcy Forchheimer porous medium. Case Stud Therm Eng. 2023;51:103642.

[36] Sharma BK, Anup Kumar NK, Mishra I, Albaijan U. Fernandez-Gamiz, Computational analysis of melting radiative heat transfer for solar Riga trough collectors of Jeffrey hybrid-nanofluid flow: A new stochastic approach. Case Stud Therm Eng. 2023;52:103658.

[37] Yasmin H, Lone SA, Mahnashi AM, Hamali W, Raizah Z, Saeed A. The electrically conducting water-based nanofluid flow containing titanium and aluminum alloys over a rotating disk surface with nonlinear thermal radiation: A numerical analysis. Open Phys. 2024;22(1):20230184.

[38] Rawat SK, Mishra A, Kumar M. Numerical study of thermal radiation and suction effects on copper and silver water nanofluids past a vertical Riga plate. Multidiscip Model Mater Struct. 2019;15(4):714–36.

[39] Das S, Mondal H, Kundu PK, Sibanda P. Spectral quasi-linearization method for Casson fluid with homogeneous heterogeneous reaction in presence of nonlinear thermal radiation over an exponential stretching sheet. Multidiscip Model Mater Struct. 2019;15(2):398–417.

[40] Sivasankaran S, Bhuvaneswari M, Amer AA. Numerical study on buoyant convection and thermal radiation in a cavity with various thermal sources and Cattaneo-Christov heat flux. Case Stud Therm Eng. 2021;27:101207. doi: 10.1016/j.csite.2021.101207.

[41] Gangadhar K, Vijayakumar D, Thangavelu K. Nonlinear radiation on Maxwell fluid in a convective heat transfer with viscous dissipation and activation energy. Heat Transf. 2021;50(7):7363–79.

[42] Mandal G, Pal D. Impact of gold and silver nanoparticles on the thermally radiating MHD slip blood flow within the stenotic artery using stability analysis and entropy optimization. Pramana – J Phys. 2024;98:157. doi: 10.1007/s12043-024-02840-0.

[43] Choudhury K, Sharma S. Natural convection MHD mass transfer through an infinite vertical porous plate in the existence of radiation embedded in porous medium. Heat Transf. 2023;53(3):1031–49.

[44] Gangadhar K, Kumari MA, Chamkha AJ. EMHD flow of radiative second-grade nanofluid over a riga plate due to convective heating: Revised Buongiorno’s nanofluid model. Arab J Sci & Eng. 2022;47:8093–103. doi: 10.1007/s13369-021-06092-7.

[45] Rashid S, Hayat T, Qayyum S, Ayub M, Alsaedi A. Three-dimensional rotating Darcy–Forchheimer flow with activation energy. Int J Numer Methods Heat Fluid Flow. 2019;29(3):935–48.